Pseudo-Rigid-Body Dynamic Models for Design of Compliant Members

Vedant[1]
Department of Aerospace Engineering,
University of Illinois at Urbana-Champaign,
Aerospace Engineering,
Urbana, IL 61801
e-mail: vedant2@illinois.edu

James T. Allison
Department of Industrial and Enterprise Systems Engineering,
University of Illinois at Urbana-Champaign,
Industrial & Enterprise Systems Engineering,
Urbana, IL 61801
e-mail: jtalliso@illinois.edu

Movement in compliant mechanisms is achieved, at least in part, via deformable flexible members, rather than using articulating joints. These flexible members are traditionally modeled using finite element analysis (FEA)-based models. In this article, an alternative strategy for modeling compliant cantilever beams is developed with the objectives of reducing computational expense and providing accuracy with respect to design optimization solutions. The method involves approximating the response of a flexible beam with an n-link/m-joint pseudo-rigid-body dynamic model (PRBDM). Traditionally, static pseudo-rigid-body models (PRBMs) have shown an approximation of compliant elements using two or three revolute joints (2R/3R-PRBM). In this study, a more general nR-PRBDM model is developed. The first n resonant frequencies of the PRBDM are matched to exact or FEA solutions to approximate the response of the compliant system and compared with existing PRBMs. PRBDMs can be used for co-design studies of flexible structural members and are capable of modeling large deflections of compliant elements. We demonstrate PRBDMs that show dynamically accurate response for a random geometry cantilever beam by matching the steady-state and frequency response, with dynamical response accuracies up to 10% using a 5R-PRBDM. [DOI: 10.1115/1.4045602]

Keywords: compliant mechanisms, multiobjective optimization, simulation-based design

1 Introduction

Many complex engineering systems are composed of multiple mechanical members to attain the desired functionality and performance. Recently, it has been shown that elastic compliance in individual members within a system can be exploited to reduce system complexity [1]. This can be achieved in part by utilizing compliance to create multifunctional components, which can help reduce the required number of discrete components. In addition, compliant mechanisms can help reduce overall volume, improve mechanical precision, and reduce wear.

Modeling such systems is a challenging task. There are several methods of varying fidelity to model the compliant members; some of the well-known methods include: finite element analysis (FEA)-based models, lumped-parameter models, and pseudo rigid body models (PRBMs) [1]. Each of these methods has been shown to have individual strengths and weaknesses. Since many compliant structures undergo large deflection, techniques that approximate the performance of the compliant structure well for large deflection are desirable. PRBMs approximate the performance of a compliant member by modeling them as a series of rigid bodies linked to each other using torsional spring joints. PRBMs have been shown to model properties such as bistability/tristability [2,3], dynamic behaviors [4,5], and pose workspace [6].

Pseudo-rigid-body dynamic models (PRBDMs) are a variation of PRBMs, where the dynamic response of the model is matched to the expected response from the complaint system. The matching of system response can be performed using several metrics. Some of the existing approaches have utilized the deflection of a compliant member (e.g., a cantilever beam) under constant structural loads. Most initial studies explored the spring stiffness and the position of a single revolute joint (1R-PRBM) to approximate the dynamics [1]. The 1R-PRBM uses a characteristic pivot along the beam, used to approximate the response of any compliant member. Subsequent studies have explored more accurate approximation of the compliant members that undergo larger deflection levels using two revolute joint (2R) [7] and 3R-PRBM models [8]. These models focused on mapping the deflection of a compliant member accurately. Most PRBMs are load-dependent, where the spring stiffness and joint position depend on the value and type of load applied. Subsequent efforts have been made to make PRBMs independent of loads [9], but these models do not account accurately for dynamic response. This is undesirable for a general model approximation. A survey of multiple PRBMs is provided in Ref. [10].

A comparison of the lumped-parameter model against the FEA results for compliant members was performed previously, and it was discovered that the lumped model was more accurate in approximating deflection, whereas the FEA model was more effective at modeling resonant frequencies [11]. This trade-off is further investigated in this study, and results demonstrate that the PRBDMs have a more accurate dynamical response. Specifically, accuracy improvement is shown with respect to both frequency response and beam tip deflection.

One type of co-design is a class of dynamic system design problems and solution methods of growing importance that aims to produce system-optimal designs by considering both physical and control system design decisions in an integrated manner [12–14]. To confusion with how the term "co-design" is used in other contexts, in this article the more specific term control co-design (CCD) is used to refer to integrated physical and control system design. Successful application of CCD methods requires the creation of low- to medium-fidelity models that predict the effect of changes both to physical and control system design decisions. Medium-fidelity models that do not depend on computationally expensive steps (e.g., re-meshing) are very desirable for CCD applications, such as compliant mechanisms and intelligent structures.

In this study, a method of modeling a non-uniform compliant cantilever beam using *n*R-link PRBDMs is introduced. The objective of the realized PRBDM is to have a similar dynamical response as the original beam. The dynamical response of a system is considered similar if the steady-state and frequency response of a system is similar [15]. The PRBDM parameters are obtained by minimizing

[1]Corresponding author.

Contributed by the Design Automation Committee of ASME for publication in the Journal of Mechanical Design. Manuscript received June 15, 2019; final manuscript received November 1, 2019; published online December 5, 2019. Assoc. Editor: Scott Ferguson.

the difference in natural resonance frequency (i.e., aim to achieve identical frequency response). Quantitative comparison of mapping strategies is based on candidate beams whose specifications are generated randomly, and where the first n eigenvalues are approximated using various methods. These approximated eigenvalues are compared against "truth" values obtained for test beams using an FEA-based eigen analysis with a high-resolution mesh. The natural frequency for this study is obtained using COMSOL [16] eigenvalue analysis, and the eigenvalue of the PRBDM equation is matched using an optimization scheme to find the system parameters that minimize the difference in the eigenvalues of the two systems. Alternate methods to obtain the resonant frequencies include the use of analytical [17] and machine learning methods. A PRBDM comparison to analytical solutions for a uniform beam is provided in the Supplemental Materials on the ASME Digital Collection.

After obtaining truth values for dynamic response, the PRDBM model parameters are optimized for two objective functions—one for matching natural resonance frequency and the other for matching deflection under structural loads (steady-state response)—using a multi-objective optimizer. The obtained results then are used to find a good metric to use to obtain dynamically accurate PRBDMs.

The study concludes with a strategy to obtain PRBDMs that can approximate dynamical response of a compliant beam, with the accuracy of the model dependent upon the number of links chosen by the user. Models that use fewer links are dynamically less accurate, but are much more computationally efficient. Such PRBDMs will support engineers in making effective trade-offs between system accuracy and computation effort, making them good candidates for CCD studies. Such studies would involve the solution of a CCD optimization problem, while increasing the number of links (and therefore model fidelity and computational expense). Investigating the effectiveness of various PRBDM mapping strategies directly in the context of CCD is a topic of ongoing work and is outside the scope of this article that focuses on introduction of an initial comparison of new PRBDM mapping strategies for more general compliant beams.

These models will be used for CCD of dynamical systems that utilize compliant members to reduce physical system complexity [5]. Strain-actuated solar arrays [18,19], multifunctional structures for attitude control [20], aeroelastic airfoil design [21], and wind turbine design are some example applications where high-strain compliant members could be used to increase system reliability and performance and reduce system cost and wear, and the models presented this article could support effective CCD optimization of these systems. Most of the systems above can be modeled as compliant cantilever beams. Hence, the PRBDM development in this article focuses primarily on cantilever beams. The benefits of a PRBDM over conventional FEA-based models is that during the process of CCD optimization, a new model will not need to be re-meshed, which is the most significant bottleneck for large problems of this class. The most important requirement for such PRBDMs for CCD optimization is to have the same dynamical response as an FEA-based model, such that the optimization solutions of both FEA (expensive) and PRBDM (inexpensive) strategies are consistent.

This paper is organized into four main sections. In Sec. 2, the PRBDM and key system performance metrics that will be used to find the design parameters are introduced. Section 3 then describes the methods used to find the best spring stiffness and joint lengths to fit the PRBDM to a "truth" model. Additionally, methods such as scaling and other techniques used to reduce the complexity of the problem are described. Next, the PRDBM model is optimized using an eigenvalue-matching objective, and obtained models are presented. Finally, a multi-objective optimization is performed to find the design parameters for the PRBDM. The optimization is performed according to two objectives: (1) eigenvalue mapping and (2) matching beam tip deflection under structural load. This yields a PRBDM that can be compared with existing PRBMs [22,23]. These obtained models are then compared for their accuracy based on the dynamical response of "truth" models (FEA solutions in the main case studies, analytical solutions for the uniform beam in the Supplemental Materials on the ASME Digital Collection). The obtained Pareto front is discussed for a candidate beam with spatially varying properties.

2 Problem Formulation

PRBDM method accuracy depends on obtaining appropriate values for spring stiffness, the number of joints, and the distance between joints. For design purposes, these model parameters must be estimated based on independent physical design variables, such as geometric parameters. The dynamical equations for an nR-PRBDM are then formulated. The cantilever beam, which is constrained to move in a 2D plane, can be approximated as an n-revolute joint rigid multi-body arm, as depicted in Fig. 1. This study quantitatively compares several mapping strategies to determine the choice of spring stiffness and node distance to best match the eigenvalues, based on geometric design parameters. Here, it is assumed that the panels have a maximum limit of 1 m for length and width, while the thickness was limited to a minimum of 10 mm. This process is summarized in Fig. 2. The top row of boxes are inputs to the method, the bottom left boxes indicate the prepossessing and scaling employed to improve the computational performance, the bottom center box is the optimization explained in Sec. 2.3, and bottom right is the PRBDM obtained.

2.1 Generating Random Candidates. The mapping strategies are tested by applying them to a cantilever beam with spatially varying properties based on randomly generated geometric design parameters. The candidate beams are generated by first declaring the number of sections in the panel, denoted as an integer p. The generation steps include:

(1) Choose p random numbers between 0 and 1, order these in ascending order, and append 0 and 1 to this list. These will serve as the X (longitudinal) coordinates for the polygon representing distributed beam geometry (similar to the piecewise-linear design description used in Ref. [18]).
(2) Next choose $p+2$ additional random real numbers between 0 and 1; these will serve as the Y (lateral) coordinates for the polygon.
(3) Define a polygon where its starting point is the origin, its endpoint is the point (0,1), and the start and end points are connected by a piecewise linear curve defined by vertices with positions specified by the ordered list of X and Y values.
(4) Reflecting the curve about the X-axis generates the closed polygon representing the planform geometry of a candidate beam.
(5) Extruding this polygon to thickness t (in the Z-direction, out of the page) yields the complete description of a randomly generated test beam.

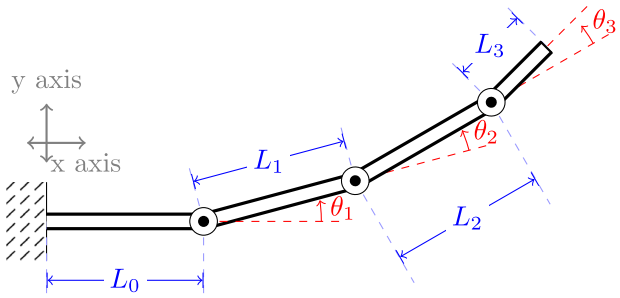

Fig. 1 Illustration of 4-link/3R PRBDM

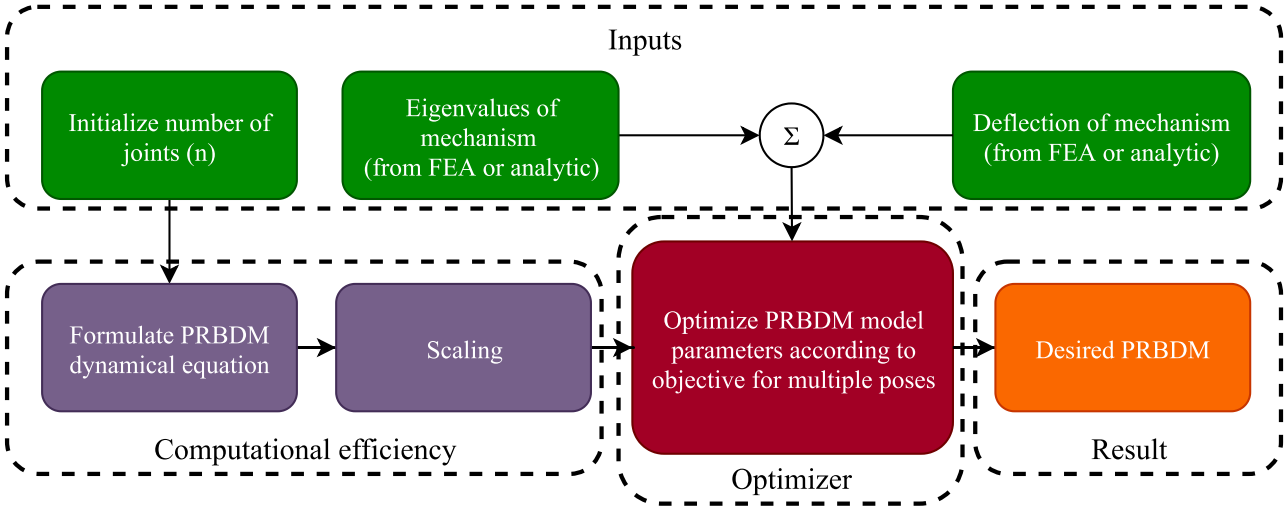

Fig. 2 Method proposed, to find model parameters for an *n*R-PRBDM

All beams used in the tests here each have a uniform thickness in the X–Y plane. One of the candidate panels is shown in Fig. 3. Changes in width influence spatially varying beam stiffness and inertia. This paper uses the same random beam that was used for a previous study, as well as many values of the PRBDM that were solved in Ref. [19].

2.2 Pseudo-Rigid-Body Dynamic Model. The dynamical model for an $(n+1)$-link/nR arm in general can be represented by Eq. (1). Assuming the beam is in a gravity-free environment, the contribution of $\mathbf{G}(\boldsymbol{\theta}, \boldsymbol{\psi})$ is defined in Eq. (2).

$$\mathbf{M}(\boldsymbol{\theta}, \boldsymbol{\psi})\ddot{\boldsymbol{\theta}} + \mathbf{C}(\boldsymbol{\theta}, \dot{\boldsymbol{\theta}}, \boldsymbol{\psi})\dot{\boldsymbol{\theta}} + \mathbf{G}(\boldsymbol{\theta}, \boldsymbol{\psi}) = \boldsymbol{\tau} \tag{1}$$

$$\mathbf{G}(\boldsymbol{\theta}, \boldsymbol{\psi}) = \mathbf{K}\boldsymbol{\theta} = \begin{bmatrix} K_{11} & \cdots & K_{1n} \\ \vdots & \ddots & \vdots \\ K_{n1} & \cdots & K_{nn} \end{bmatrix} \theta \tag{2}$$

In the above equations, θ and $\dot{\theta}$ are the local relative angular positions and velocities for each link. The quantities q and $\dot{q}$ correspond to the angular orientation and velocity of each link with respect to the global/world frame. The vector τ indicates the torque applied at each joint, and ψ is the vector of design parameters for all links. Figure 1 shows an example of a 4 link/3R-PRBDM. Here, θ_n is the relative angle of the nth link with respect to the $(n-1)$th link. The relationship between θ and q is shown in Eq. (3). The first link is always aligned to the world X-axis, as quantified in Eq. (4), resulting in a non-singular stiffness matrix K.

$$\theta_j = q_j - q_{j-1}, \quad \forall\, j \in [1, 2, \ldots, n] \tag{3}$$

$$q_0 = 0 \tag{4}$$

The matrix $C(\theta, \dot{\theta}, \psi)$ in Eq. (1) represents the Coriolis effect of the system. In addition, an artificial quasi-empirical (C_{qe}) damping term is added to the Coriolis term to render the model more tractable for simulation, similar to Ref. [11]. Ongoing work is addressing the inclusion of designed distributed damping (e.g., viscoelastic treatments) for PRBDMs of compliant beams [24]. Here, damping is included only for numerical simulation enhancement. The modified $\mathbf{C}_m(\boldsymbol{\theta}, \dot{\boldsymbol{\theta}}, \boldsymbol{\psi})$ with damping is defined in Eq. (5):

$$\mathbf{C}_m(\boldsymbol{\theta}, \dot{\boldsymbol{\theta}}, \boldsymbol{\psi}) = \boldsymbol{C}(\boldsymbol{\theta}, \dot{\boldsymbol{\theta}}, \boldsymbol{\psi}) + \boldsymbol{C}_{qe}(\boldsymbol{\theta}, \dot{\boldsymbol{\theta}}, \boldsymbol{\psi}) \tag{5a}$$

$$\mathbf{C}_{qe}(\boldsymbol{\theta}, \dot{\boldsymbol{\theta}}, \boldsymbol{\psi}) = 2\boldsymbol{M}(\boldsymbol{\theta}, \boldsymbol{\psi})\boldsymbol{\xi}\boldsymbol{\lambda} \tag{5b}$$

$$\mathbf{C}_{qe}(\boldsymbol{\theta}, \dot{\boldsymbol{\theta}}, \boldsymbol{\psi}) = 2\begin{bmatrix} \xi_1 & 0 & 0 \\ 0 & \ddots & 0 \\ 0 & 0 & \xi n \end{bmatrix} (\mathbf{M}(\boldsymbol{\theta}, \boldsymbol{\psi})\mathbf{K})^{1/2} \tag{5c}$$

where $\xi_1, \ldots, \xi_n$ are the damping factors for each joint, and λ are the eigenvalues of the PRBDM. The eigenvalues (λ) of the PRDBM model can be calculated using Eq. (6):

$$\boldsymbol{\lambda}^2 = (\mathbf{M}(\boldsymbol{\theta}, \dot{\boldsymbol{\theta}}, \boldsymbol{\psi}))^{-1}\mathbf{K} \tag{6}$$

The effective torques on each joint due to an external force (F_{ext}) can be calculated using Eq. (7):

$$\tau = \mathbf{J}^{\mathbf{T}}(\boldsymbol{\theta}, \boldsymbol{\psi})\mathbf{F}_{\text{ext}} \tag{7}$$

where $\mathbf{J}^{\mathbf{T}}$ is transpose of the Jacobian for the PRBDM from the tip to the base. The steady-state tip deflection of the nR-PRBDM due to an external force on the beam can be calculated by solving Eq. (8) for θ [25]. We obtain Eq. (8) by imposing steady-state conditions ($\dot{\theta} = 0$ and $\ddot{\theta} = 0$) on Eq. (1):

$$\mathbf{G}(\boldsymbol{\theta}, \boldsymbol{\psi}) = \mathbf{K}\boldsymbol{\theta} = \mathbf{J}^{\mathbf{T}}(\boldsymbol{\theta}, \boldsymbol{\psi})\mathbf{F}_{\text{ext}} \tag{8}$$

The beam tip deflection of the PRDBM can be estimated by solving Eq. (9):

$$\boldsymbol{\theta} = K^{-1}J^{T}(\theta, \psi)F_{\text{ext}} \tag{9a}$$

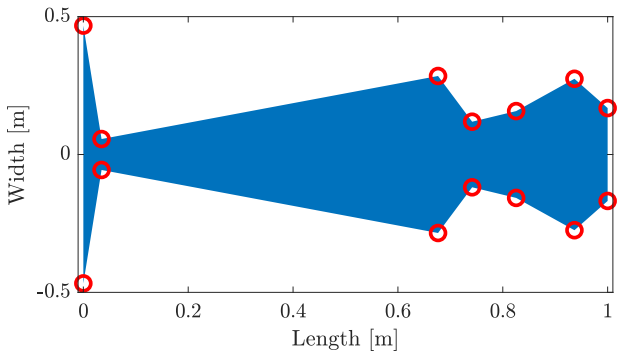

Fig. 3 Visualization of a randomly generated beam, symmetric about the horizontal axis. Planform geometry shown; vibrations and deflections occur out-of-plane.

$$\mathbf{P}_{PRBDM} = F(\theta) \tag{9b}$$

Here, P_{PRBDM} is the position vector of the cantilever beam tip under some known structural load, and $F(\theta)$ is the forward kinematics model for the PRDBM.

2.3 Mapping Strategies. In this study, two different mapping strategies are studied and compared for a cantilever beam. The objective of these strategies is to find the PRBDM parameters (spring stiffness and link length values) for a given geometric beam design such that the resonance frequencies (eigenfrequencies) and steady tip deflection for the PRBDM matches that of the continuous compliant beam.

This section introduces scaling strategies and other constraints that will be used for both mapping strategies. These support solution of the corresponding model parameter optimization problem with greater computational efficiency.

2.3.1 Mapping Preliminaries. Numerical optimization is used to minimize the mapping objectives for an $(n+1)$-link/nR-PRBDM based on truth values. The optimizer chooses the distance between the nodes L_j and each joint stiffness K_j, $j = 1, \ldots, n$, where n is the number of joints.

A core challenge in this modeling problem is that the joint stiffnesses and eigenvalues depend on position via mass matrix dependence on the pose. As a strategy to manage this variation in eigenvalues, we calculate for each design the eigenvalues across a range of poses. We generate this set of poses by sweeping across a range of joint position values θ_i from small angles (ϵ) to $\pi/2$, as depicted in Eq. (10):

$$\hat{\theta}_i = A_{i,\langle\cdot\rangle} \tag{10}$$

where $\hat{\theta}_i$ is the vector of all joint angles for pose i, and $A_{i,j}$ is an $m \times n$ matrix where the ith row corresponds to $\hat{\theta}_i$. Specifically,

$$A_{i,\langle\cdot\rangle} = [\xi + i\epsilon, \ldots, \xi + i\epsilon] \tag{11}$$

where ξ is small scalar offset value to prevent singular M (discussed below) and ϵ is the small fixed angular value. Here, ϵ is chosen such that at the mth pose, the end link world angle q_n is close to (but not exceeding) $\pi/2$. Specifically, in the implementation here, $\epsilon = \pi/2n$. Other definitions of ϵ are possible.

The model given in Eq. (1) was not tested for any cases where $\theta = 0$, as this would result in a singular mass matrix (M) [26]. The pose for the PRBDM for the two boundary cases of $A_{0,\langle\cdot\rangle}$ and $A_{m,\langle\cdot\rangle}$ is shown in Fig. 4.

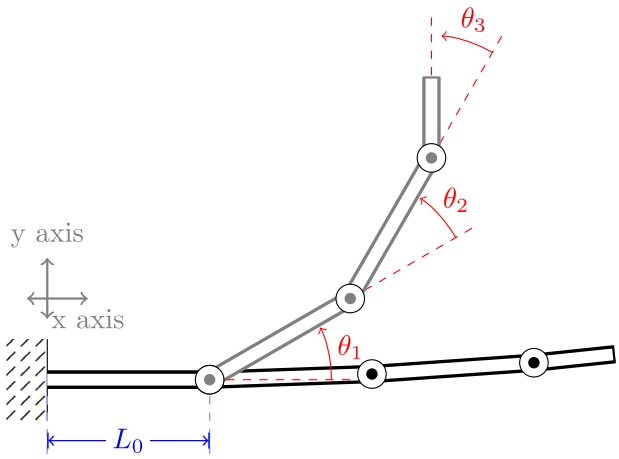

Fig. 4 A 3R PRBDM at two different poses. The gray pose is the position with $\theta = \xi + \zeta\epsilon \times$ ones(1, 3), and the black pose corresponds to $\theta = \xi \times$ ones(1, 3).

In the most general case, the stiffness of each joint is a continuous function of pose θ. To approximate this relationship in a discrete way, we define m different stiffness values for each joint. This results in $n \times m$ joint stiffness values required to specify a design.

In this study, a reduced-dimension stiffness representation is employed where a single stiffness correction parameter is found that allows us to define a single-independent stiffness parameter for each joint, which then maps to m unique stiffness values for each joint for each pose. The rationale for this approach is that the stiffness variation on pose is modeled as a material property.

More specifically, the stiffness matrix in Eq. (2) is assumed to be a diagonal matrix, as shown in Eq. (12):

$$K = \begin{bmatrix} K_{11} & 0 & \cdots & 0 \\ 0 & K_{22} & \ddots & \vdots \\ \vdots & \ddots & \ddots & 0 \\ 0 & \cdots & 0 & K_{nn} \end{bmatrix} \tag{12}$$

To define an initial design for optimization, a unique K is assumed for each unique pose i of the same form as Eq. (12). This yields m stiffness matrices; the elements of these m matrices are defined according to Eq. (13):

$$\hat{K}_i = \begin{bmatrix} K_{11}(i) & 0 & \cdots & 0 \\ 0 & K_{22}(i) & \ddots & \vdots \\ \vdots & \ddots & \ddots & 0 \\ 0 & \cdots & 0 & K_{nn}(i) \end{bmatrix} \tag{13}$$

$\hat{K}_i$ quantifies the stiffness for pose i, where the spring stiffness for each joint j and pose i, $K_{jj}(i)$, is approximated using a linear scaling to reduce the design representation dimension, according to Eq. (14):

$$K_{jj}(i) = k_i \times \sqrt{\frac{EI_j}{\hat{m}_j}} \tag{14}$$

where k_i is defined as a scaling parameter, also referred as stiffness correction factor, that is used as the independent stiffness design variable approximates how joint stiffness depends on pose. E is the material modulus of elasticity, I_j is the area moment of inertia (I_{yy}) for link j, and $\hat{m}_j$ is the mass of link j. This linear mapping strategy uses m independent design variable values for k_i, along with link mechanical properties, to generate $n \times m$ unique stiffness variables needed to define $\hat{K}_i$, $i = 1, \ldots, m$. Equation (12) is based on the assumption that the stiffness correction factor is a characteristic of the material and should not depend on the properties unique to each section. The corresponding optimization problem for model parameter mapping is

$$\min_{L_j, k_i} \quad \sum_{i=1}^{m} \mathbf{f}_{error}(\boldsymbol{\theta}_i, \dot{\boldsymbol{\theta}}_i, \boldsymbol{\psi}) \tag{15a}$$

$$\text{subject to:} \quad \sum_{j=0}^{n} L_j = 1 \tag{15b}$$

$$L_j \geq 0.02, \tag{15c}$$

$$L_j \leq (1 - 0.02) \tag{15d}$$

where L_j is the length of the jth link (these values are independent of the pose) and $f_{error}(\cdot)$ is the error metric either based on eigenfrequency or deflection error (defined in detail below).

2.3.2 Eigenfrequency-Based Mapping. The eigenfrequencies for the randomly generated beams are obtained using COMSOL eigenvalue analysis. The eigenvalues and the mass participation

factors are saved. The eigenvalues that have the highest mass participation in the deflection direction are filtered and arranged in ascending order. The optimizer reduces the difference between the sorted eigenvalues from PRBDM (Eq. (6)) and FEA-based systems by minimizing the ℓ_2 norm between the sorted eigenvalue vectors, as defined in Eq. (16):

$$\boldsymbol{\lambda}_{error}(\boldsymbol{\theta}_i, \dot{\boldsymbol{\theta}}_i, \boldsymbol{\psi}) = \frac{\|\boldsymbol{\lambda}_{\mathbf{FEA}} - \boldsymbol{\lambda}_{PRBDM}(\boldsymbol{\theta}_i, \dot{\boldsymbol{\theta}}_i, \boldsymbol{\psi})\|_2}{\|\boldsymbol{\lambda}_{FEA}\|_2} \tag{16}$$

Here, it is assumed that $\dot{\theta}_i = 0$. The objective is normalized to aid to comparison to the deflection error metric. The optimization problem formulation for eigenvalue matching is defined in Eq. (15), where $\mathbf{f}_{error}$ is defined according to Eq. (17).

$$\mathbf{f}_{error}(\boldsymbol{\theta}_i, \dot{\boldsymbol{\theta}}_i, \boldsymbol{\psi}) = \boldsymbol{\lambda}_{error}(\boldsymbol{\theta}_i, \mathbf{0}, \boldsymbol{\psi}) \tag{17}$$

2.3.3 Deflection-Based Mapping. The second objective for finding the spring stiffness and the optimal link lengths is also formulated as an optimization problem. The stationary deflection solver from COMSOL is used to estimate the deflection of the beam under different forces P_{FEA}. This then allows us to define a second objective function based on a comparison between the PRDBM tip deflection Eq. (9) and the FEA model. It must be noted, however, that solving Eq. (9*a*) cannot be performed analytically, due to the dependence of the Jacobian on θ. The deflection error metric uses the ℓ_2 norm of the difference in the tip position between the two models:

$$\mathbf{f}_{error}(\boldsymbol{\theta}_i, \dot{\boldsymbol{\theta}}_i, \boldsymbol{\psi}) = \boldsymbol{\delta}_{error}(\boldsymbol{\theta}_i, \dot{\boldsymbol{\theta}}_i, \boldsymbol{\psi}) \tag{18}$$

$$\boldsymbol{\delta}_{error}(\boldsymbol{\theta}_i, \dot{\boldsymbol{\theta}}_i, \boldsymbol{\psi}) = \frac{\|\mathbf{P}_{\mathbf{FEA}} - \mathbf{P}_{PRBDM}(\mathbf{F}_{ext})\|_2}{\|\mathbf{P}_{FEA}\|_2} \tag{19}$$

The objective is normalized to the FEM "truth" value, thereby making it easier to compare. This objective function can then be used with the optimization problem given in Eq. (15).

The eigenvalue mapping objective is solved using the MATLAB[2] function `fmincon` with `MultiStart` to improve the probability of finding globally-optimal PRBDM parameter values. Subsequently, a multi-objective `paretosearch` is performed using the two normalized objectives, Eqs. (15) and (19).

2.4 Model Parameter Calculation. The compliant beam model parameter vector ψ is a vector of length $(5+m)\times n$. Equation (20) details the components of ψ:

$$\boldsymbol{\psi} = [\boldsymbol{\gamma}, \mathbf{k}, \hat{\mathbf{m}}, \mathbf{I}_{\text{yy}}, \mathbf{X}_{\text{com}}, \mathbf{Y}_{\text{com}}]^{\text{T}} \tag{20}$$

where γ is a vector (length n) of normalized link length values:

$$\gamma_i = L_i / L_{\text{total}}, \quad L_{\text{total}} = \sum_i L_i = 1 \tag{21}$$

k is a vector (length m) of stiffness correction factors for each pose, $\hat{m}$ is a vector (length n) containing the mass of each link (assuming constant cross-section prismatic geometry), I_{yy} is the vector of rotational mass moments of inertia for each link, and X_{com} and Y_{com} are the center-of-mass locations in the $n-1$th joint frame. Due to the symmetry assumption used here, all values for the vector Y_{com} are zero (at least with respect to numerical tolerances).

Once the number of joints has been chosen for the PRBDM to approximate the compliant member, independent components of ψ can be specified:

$$\boldsymbol{\psi}_{\text{ind}} = [\boldsymbol{\gamma}, \mathbf{k}]^{\mathbf{T}} \tag{22}$$

These are the $(n+m)$ independent model parameter optimization variables based on the above PRBDM approximation and linear stiffness correction strategy. The remaining model parameters in ψ are calculated from ψ_{ind}. Once ψ_{ind} is specified, the optimization problem given in Eq. (15) is solved using a multi-start approach with a gradient-based optimization algorithm. The set of start points are generated using a custom strategy, defined in Eq. (23):

$$L = \text{random}(1{,}100, n-1) \tag{23a}$$

$$\gamma = \left[L, 1 - \sum L\right]^{\text{T}} \Big/ 100 \tag{23b}$$

$$k = \text{random}(m) \tag{23c}$$

where $L = [L_1, \ldots, L_{n-1}]$ is the vector of link lengths, random(·) is a uniform pseudo-random number generator without replacement, γ is a normalized length vector based on the random length vector, and k is a randomly generated set of stiffness correction factors (length m). The numerical scaling defined in Eq. (14) eases numerical solution difficulty due to differing orders of magnitude in the unscaled parameter space. In Eq. (23*a*), the random function chooses $n-1$ unique random integers between 1 and 100. To sample a random uniform distribution under the simplex condition (Eq. (15*b*)), the method described in Ref. [28] is used, as seen in Eq. (23*b*).

Once the values of γ and k are known, the values of $\hat{m}$, I_{xx}, I_{yy}, X_{com}, and Y_{com} can be estimated using the first- and second-area moments of the polygon sections. During the optimization, for each new link length design γ, the physical properties for each link are calculated, and an updated ψ is obtained. The physical properties for each section are shown in Fig. 5 for a sample design.

3 Test Problems

In this section, the randomly generated cantilever beam is modeled using the PRBDM defined above. The material for the beam is Steel ANSI 4340, available in COMSOL [16]. The PRBDM model for 4-link and 5-link cases is used as candidate models to match the first 4 (and 5) modes. The optimal stiffness correction factor k_i and joint separation L_j are obtained by solving the optimization problem in Eq. (15) using the algorithm settings shown in Table 1.

A random beam is generated using the procedure stated in Sec. 2, for $p = 10$. The randomly generated beam used for the studies presented here is shown in Fig. 3. COMSOL was used to estimate the first 40 natural frequencies for the beam along with the mass participation factors (MPFs) for each mode. A high-resolution mesh is used to estimate the resonant frequencies, as shown in Fig. 6, according to the parameters presented in Table 2. The coarse mesh supports computationally efficient estimation of the resonant frequencies. The resonant frequencies are then filtered according to the MPF to obtain the modes that exhibit bending along the desired axis. The vector of five eigenvalues obtained for the panel from Fig. 3, using the mesh shown in Fig. 6, is presented in Eq. (24).

$$\boldsymbol{\lambda}_{panel} = [48.342, 359.4, 1013.5, 5711.4, 7816]^{\text{T}} \tag{24}$$

The multi-objective optimization algorithm is solved for the same beam using 4-link (3R), 5-link (4R), and 6-link (5R) PRBDMs. The ϵ (Eq. (11)) for the Pareto-front search was set to 0.01 radians, much smaller than the single objective, allowing for a more detailed solution for more configurations of the PRBDM. The optimization solver parameters listed in Table 1 were used.

4 Results and Discussion

In this section, first the results for the single objective optimization study are discussed and then the multi-objective results are presented. The first case performs mappings for randomly generated beams. The PRBDM matching code, which is available at

[2]The MATLAB code for these test problems is available in Ref. [27].

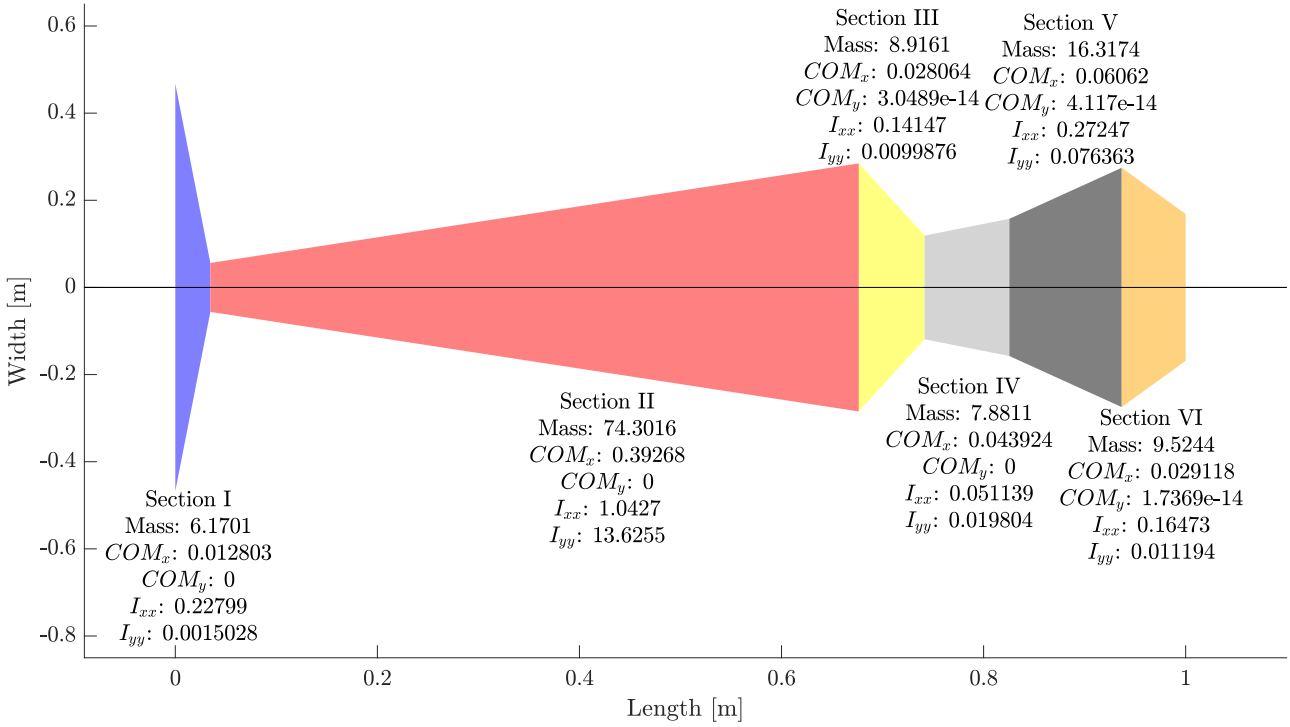

Fig. 5 Plot of randomly generated beam, with physical properties for each section (link)

Table 1 Optimization solver settings

Algorithm	`fmincon`, `MultiStart` [29–31]	`ParetoSearch` [32–34]
Constraint tolerance	1×10^{-6}	1×10^{-9}
Step tolerance	1×10^{-6}	1×10^{-6}
Max iterations	10000	$4000\times(5+\text{m})\times\text{n}$
Optimality tolerance	1×10^{-6}	–
Max function evaluations	5000	$12{,}000\times(5+\text{m})\times\text{n}$
ϵ (Eq. (11))	0.01	0.01

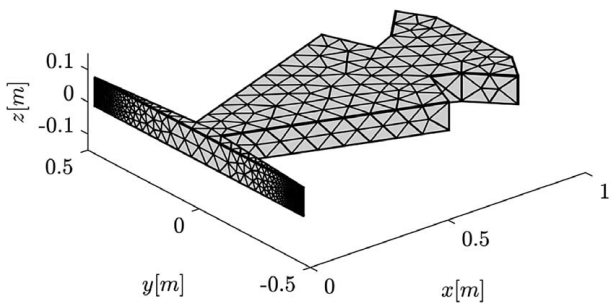

Fig. 6 Mesh for random panel used for FEM analysis

Ref. [27], was solved for 50,000 different model beams; the beam discussed here is beam number 17,572.[3] The beam was modeled using a 4R-PRBDM and a 5R-PRBDM for a different number of eigenvalues.

[3]The remaining data will be available upon final publication via an archival data repository.

Table 2 Mesh generation parameters [16]

Maximum element size	0.03 m
Minimum element size	0.001 m
Maximum element growth rate	1.5
Curvature factor	0.3
Resolutions of narrow regions	0.9

4.1 Single Objective Optimization—Eigenvalue Mapping. The random beam was solved for both the 4R-PRBDM and the 5R-PRBDM cases. Both cases were solved to map the first three eigenfrequencies as well as the maximum number of eigenfrequencies that the models allow. The results for the random beam are thus divided into two sections, one for the 4R-PRBDM and the latter for the 5R-PRBDM.

4.1.1 4R-PRBDM Approximation. The optimization problem to solve for the spatial joint distribution and spring stiffnesses was initialized using 1024 unique initial points and solved using the `MultiStart` algorithm in MATLAB. One of the initial beam designs is illustrated in Fig. 5. The ϵ value chosen for this study was 0.1 and ξ is 0.05 for Eq. (10).

The optimizer solves for both the link lengths and SCFs simultaneously to best match the eigenvalues. For the 4R-PRBDM, the optimizer converged to the solution shown in Fig. 7. The obtained PRBDM has eigenvalues which differ by 0.033% of the eigenvalues obtained using `COMSOL`. A second case, which maps three eigenfrequencies using a 4R-PRBDM, was also tested. The three eigenvalues were mapped to an accuracy to 0.015%. A summary of optimized independent model parameters is provided in Table 3.

The length fraction for both cases of the 4R-PRBDM (γ_1) is indicative of a "characteristic pivot" for this non-uniform and higher-dimensional (4R-PRBDM) case. The right-hand side y-axis shows the percent difference between the SCF for the given joint angles to the mean SCF. The mean SCF is defined by Eq. (25). The

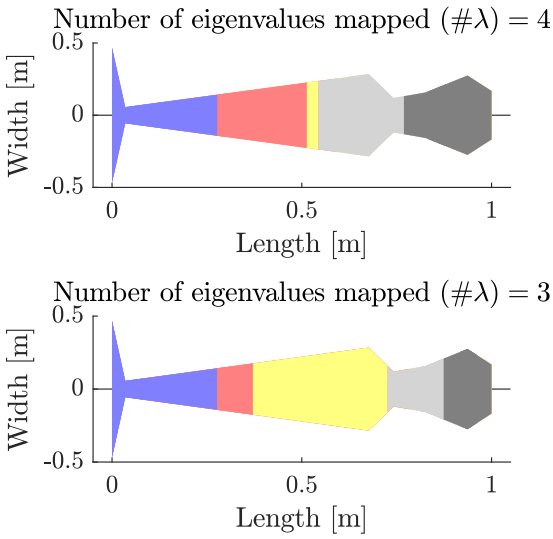

Fig. 7 Plot of a randomly generated beam with model parameters optimized for eigenvalue matching (4R-PRBDM)

variation of the spring stiffness is small, but shows a close to a linear trend.

$$\text{SCF}_{\text{mean}} = \frac{1}{m}\sum_{i=0}^{m} k_i \tag{25}$$

$$P_i = \frac{k_i - \text{SCF}_{\text{mean}}}{\text{SCF}_{\text{mean}}} 100 \tag{26}$$

The SCF for each deflection case is shown in Fig. 8. A linear trend is observed for the correction factor with respect to the angle of deflection between each link. When the SCF is applied according to Eq. (14), the spring stiffness is obtained for different deflection angles.

4.1.2 5R-PRBDM Approximation. For the 5R-PRBDM, the optimizer converged to the solution shown in Fig. 9. The obtained PRBDM has eigenvalues which differ by 0.0283% of the eigenfrequencies obtained using COMSOL. This is a better map than a 4R-PRBDM, although the 5R-PRBDM maps five eigenfrequencies instead of 4. For a more direct comparison between the 4R-PRBDM and 5R-PRBDM, three eigenfrequencies are mapped using a 5R-PRBDM, the accuracy of the model is within 0.01%. The SCF for each deflection case is shown in Fig. 10. Although a similar linear trend is observed for the correction factor with respect to the angle of deflection between each link, as with the 4R case, the variation is significantly smaller. A summary of optimized independent model parameters is presented in Table 4.

Table 3 Results for 4R-PRBDM, random beam

Frequencies mapped	SCF_{mean}	Joint distance (m)	Loss (%)
4	5.3145	$\begin{bmatrix}0.2778\\0.2354\\0.0308\\0.2250\\0.2309\end{bmatrix}$	0.0327
3	2.1469	$\begin{bmatrix}0.2773\\0.0939\\0.3549\\0.1477\\0.1262\end{bmatrix}$	0.0151

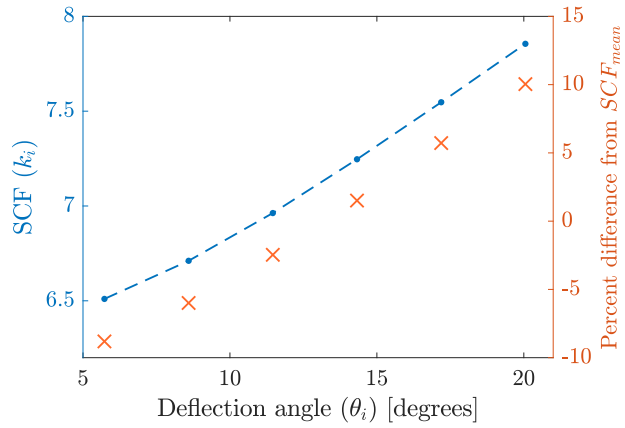

Fig. 8 Plot of the spring stiffness correction factor (SCF) versus deflection angle (in degrees), for the 4R-PRBDM random beam case. The right-hand axis corresponds to the relative change from mean values (Eq. (26)).

4.2 Multi-objective Optimization. In this section, the optimization of the models is performed using both objectives, eigenvalues and tip deflection, as defined in Eqs. (16) and (9), respectively. This is done for the 3R, 4R, and 5R PRBDM cases. The optimization problem yields a Pareto-front that is presented in Fig. 11.

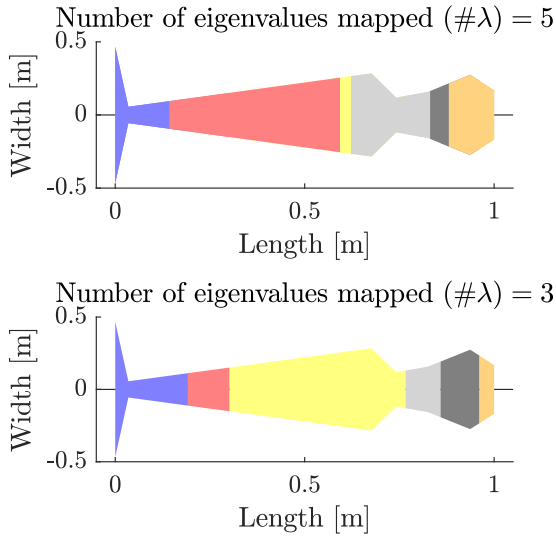

Fig. 9 Plot of a randomly generated beam with model parameters optimized for eigenvalue matching (5R-PRBDM)

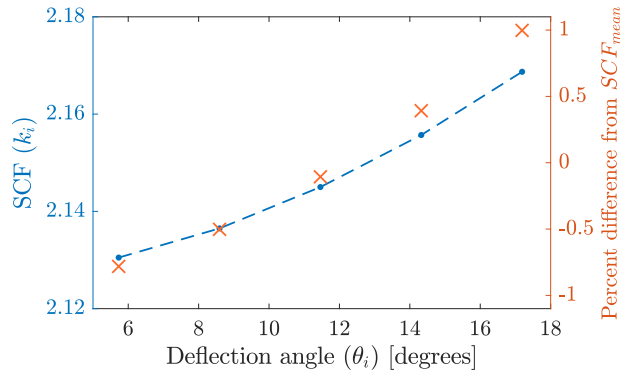

Fig. 10 Plot of spring stiffness correction factor (SCF) versus deflection angle (in degrees), for the 5R-PRBDM random beam case

Table 4 Results for 5R-PRBDM, random beam

Frequencies mapped	SCF_{mean}	Joint distance (m)	Loss (%)
5	10.5298	$\begin{bmatrix}0.1429\\0.4505\\0.0288\\0.2089\\0.0493\\0.1196\end{bmatrix}$	0.0283
3	2.6642	$\begin{bmatrix}0.1919\\0.1100\\0.4646\\0.0922\\0.1027\\0.0387\end{bmatrix}$	0.0101

Figure 11 shows the mapping accuracy of the optimal designs. The 5R-PRBDM has lower error than the 4R-PRBDM, and the 4R-PRBDM has significantly lower error than the 3R-PRBDM, as expected. The curve obtained for both the 3R-PRBDM and 4R-PRBDM models shows that optimizing the independent design parameters (ψ_{ind}) only using one objective leads to large errors in the deflection metric. The 5R-PRDBM model has low errors across the Pareto front, but it can also be seen that the 5R-PRBDM solutions perform much better for the tip deflection even when only optimized for eigenvalue mapping. Hence, having a larger number of joints/links increases the accuracy of the PRBDM for all objectives, without explicitly optimizing for them.

For the 4R-PRBDM Pareto front, the right triangle (▷) marker shows one anchor point of the Pareto front using the 4R-PRBDM, the design that maps the design parameters considering only the eigenvalue objective (Eq. (16)). The left triangle marker (◁) shows the other anchor point of the 4R-PRBDM, where the mapping is according to the tip deflection objective only (Eq. (19)). To obtain an accurate PRBDM without increasing the number of joints/links, a combination of the two objective functions will be necessary to obtain a model that has the same dynamic response as the FEA-based model. Since a dynamical model will need to map both steady-state behavior and frequency response behavior, the most dynamically accurate 4R-PRBDM

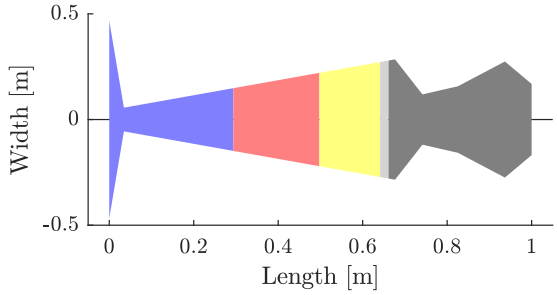

Fig. 12 Plot of randomly generated beam with model parameters optimized for dynamical response (4R-PRBDM)

(star marker, ☆) is the one closest to the origin. The closeness to the origin is with respect to the ℓ_2 norm of both objectives, as represented in Eq. (27).

$$f_{error}(\theta_i, \dot{\theta}_i, \psi) = \sqrt{\delta^2_{error} + \lambda^2_{error}(\theta_i, 0, \psi)} \tag{27}$$

It should be noted here that if the purpose of a PRBDM is to solve a CCD problem efficiently and accurately, that these two error metrics are proxy objective functions for CCD solution accuracy. The number of links, as well as the complexity of model parameter identification, are proxy objectives for CCD solution expense. More accurate evaluation of these PRBDM models in the context of benefit for CCD will require studies that quantify CCD solution properties (accuracy and expense) using a range of CCD test problems directly. This is a topic of ongoing work and is outside the scope of this article (which focuses on the fundamentals of the mapping strategies).

The panel obtained from this optimization is illustrated in Fig. 12. For comparison, the optimal design realized for the 5R-PRBDM using the same objective Eq. (27) gives the solution denoted by the square marker (■), and by the upright triangle (△) for the 3R-PRBDM in Fig. 11. Although the solution for the 5R-PRBDM seems to be farther from the origin than the solution for the 4R-PRBDM, it must be noted that the aspect ratio for the two axes is not similar, and therefore, the loss for the two are 10.2% and 13%, respectively. These comparisons and corresponding SCF_{mean} and joint separation are presented in Table 5.

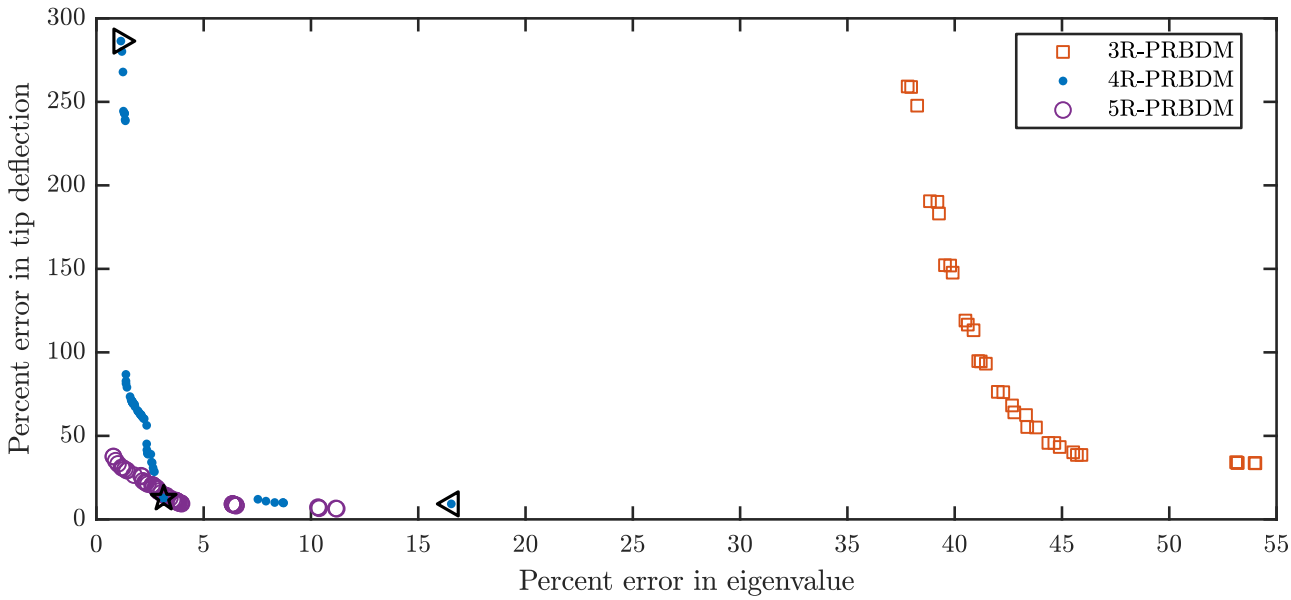

Fig. 11 Pareto front obtained from multi-objective optimization of PRBDM parameters

Table 5 Results for combined objective 4R-PRBDM and 5R-PRBDM, random beam

Model-type mapped	3R-PRBDM	4R-PRBDM	5R-PRBDM
Frequencies mapped	3	4	5
SCF_{mean}	10.2578	71.3214	97.3296
Join distance (m)	$\begin{bmatrix}0.2144\\0.6069\\0.1119\\0.0669\end{bmatrix}$	$\begin{bmatrix}0.2938\\0.2038\\0.1438\\0.0200\\0.3388\end{bmatrix}$	$\begin{bmatrix}0.1556\\0.2756\\0.1856\\0.0200\\0.3056\\0.0576\end{bmatrix}$
Loss (%)	59.8087	12.9613	10.1844

5 Conclusion and Future Work

In this article, a strategy to approximate the dynamic behavior of compliant members using a reduced-order model was presented. These PRBDMs are particularly useful for design optimization, as the computational expense can be reduced significantly while maintaining reasonable accuracy. Quantification of this trade-off with respect to design solution accuracy is a topic for future work. Two test cases are presented, but the method has been validated for a large variety of beam designs. These results and the associated code are available at Ref. [27]. Some preliminary correlation of the spring stiffness is seen with the deflection angles, and the stiffness scaling was sufficient for a linear correlation between the stiffness correction factor and deflection angles. Some evidence of characteristic pivot distances has also been observed for both the uniform beam and the random beam cases. The correlation of the joint distances with the beam shape needs further investigation to understand this relationship more deeply.

More extensive studies that optimize the reduced-order PRBDMs for an enumerated distribution of joint separation could help generate empirically driven analytic rules to determine link lengths and spring stiffness factors. If validated, this would eliminate the need to solve an optimization problem based on truth data, speeding up the implementation of effective PRBDMs for design studies. An efficient method for estimating the resonant frequencies could be obtained using a machine learning framework. Additionally, a reinforcement learning method could be used to train a neural network to provide the joint separation and spring stiffness for PRBDMs across a range of designs.

To obtain a full-fidelity, dynamically accurate PRBDM, the damping forces represented by C_{qe} (Eq. (5)) should be obtained to match the energy dissipation rate of the PRBDM to real-world examples.

In this article, model parameters were solved to minimize dynamical response error, measured by the difference in beam tip deflection and natural frequency. A model based on minimizing dynamical response error would not necessarily yield the same optimal design as that of the truth model for a system. Subsequent studies would explore finding model parameters based on optimal design results from a truth model and define design metrics that yield the same results using PRBDMs. Developing a model based on design metrics would help evaluate the potential of PRBDMs to serve as computationally efficient models for optimal CCD.

Acknowledgment

This material is based upon work partially supported by the National Science Foundation under Grant No. CMMI-1653118 and partially through a NASA SBIR in collaboration with CU aerospace (Contract No. NNX17CA25P). This work made use of the Illinois Campus Cluster, a computing resource that is operated by the Illinois Campus Cluster Program, in conjunction with the National Center for Supercomputing Applications (NCSA), and which is supported by funds from the University of Illinois at Urbana-Champaign. The authors would also like to thank Daniel R. Herber for his guidance with this study.

References

[1] Howell, L. L., 2001, *Compliant Mechanisms*, John Wiley & Sons.
[2] Jensen, B. D., and Howell, L. L., 2003, "Identification of Compliant Pseudo-Rigid-Body Four-Link Mechanism Configurations Resulting in Bistable Behavior," ASME J. Mech. Des., **125**(4), pp. 701–708.
[3] Chen, G., Wilcox, D. L., and Howell, L. L., 2009, "Fully Compliant Double Tensural Tristable Micromechanisms (DTTM)," J. Micromech. Microeng., **19**(2), p. 025011.
[4] Lyon, S., Erickson, P., Evans, M., and Howell, L., 1999, "Prediction of the First Modal Frequency of Compliant Mechanisms Using the Pseudo-Rigid-Body Model," ASME J. Mech. Des., **121**(2), pp. 309–313.
[5] Yu, Y.-Q., Howell, L. L., Lusk, C., Yue, Y., and He, M.-G., 2005, "Dynamic Modeling of Compliant Mechanisms Based on the Pseudo-Rigid-Body Model," ASME J. Mech. Des., **127**(4), pp. 760–765.
[6] Midha, A., Howell, L. L., and Norton, T. W., 2000, "Limit Positions of Compliant Mechanisms Using the Pseudo-Rigid-Body Model Concept," Mech. Mach. Theory., **35**(1), pp. 99–115.
[7] Kimball, C., and Tsai, L.-W., 2002, "Modeling of Flexural Beams Subjected to Arbitrary End Loads," Trans.-Am. Soc. Mech. Eng. J. Mech. Des., **124**(2), pp. 223–235.
[8] Su, H.-J., 2009, "A Pseudorigid-Body 3R Model for Determining Large Deflection of Cantilever Beams Subject to Tip Loads," ASME J. Mech. Rob., **1**(2), p. 021008.
[9] Venkiteswaran, V. K., and Su, H.-J., 2018, "A Versatile 3R Pseudo-Rigid-Body Model for Initially Curved and Straight Compliant Beams of Uniform Cross Section," ASME J. Mech. Des., **140**(9), p. 092305.
[10] Chen, G., Xiong, B., and Huang, X., 2011, "Finding the Optimal Characteristic Parameters for 3R Pseudo-Rigid-Body Model Using An Improved Particle Swarm Optimizer," Precision Eng., **35**(3), pp. 505–511.
[11] Chudnovsky, V., Mukherjee, A., Wendlandt, J., and Kennedy, D., 2006, "Modeling Flexible Bodies in SimMechanics," MatLab Digest, **14**(3), pp. 1–11.
[12] Fathy, H. K., Reyer, J. A., Papalambros, P. Y., and Ulsov, A., 2001, "On the coupling between the plant and controller optimization problems," Proceedings of the 2001 American Control Conference. (Cat. No. 01CH37148), Vol. 3, IEEE, New York, pp. 1864–1869.
[13] Allison, J. T., and Herber, D. R., 2014, "Multidisciplinary Design Optimization of Dynamic Engineering Systems," AIAA J., **52**(4), pp. 691–710.
[14] Herber, D. R., and Allison, J. T., 2019, "Nested and Simultaneous Solution Strategies for General Combined Plant and Control Design Problem," ASME J. Mech. Des., **141**(1), p. 011402.
[15] Ljung, L., 1999, "System Identification," Wiley Encyclopedia of Electrical and Electronics Engineering, pp. 1–19.
[16] COMSOL AB. COMSOL Multiphysics v. 5.3. Accessed June 10, 2019.
[17] Herrera-May, A. L., Aguilera-Cortés, L. A., Plascencia-Mora, H., Rodríguez-Morales, Á. L., and Lu, J., 2011, "Analytical Modeling for the Bending Resonant Frequency of Multilayered Microresonators With Variable Cross-Section," Sensors, **11**(9), pp. 8203–8226.
[18] Chilan, C. M., Herber, D. R., Nakka, Y. K., Chung, S.-J., Allison, J. T., Aldrich, J. B., and Alvarez-Salazar, O. S., 2017, "Co-Design of Strain-Actuated Solar Arrays for Spacecraft Precision Pointing and Jitter Reduction," AIAA J., **55**(9), pp. 3180–3195.
[19] Vedant, and Allison, J. T., 2019, "Pseudo-Rigid Body Dynamic Modeling of Compliant Members for Design," ASME International Design Engineering Technical Conferences and Computers and Information in Engineering Conference. Volume 2A: 45th Design Automation Conference, Anaheim, CA, Aug. 18–21, p. V02AT03A013.
[20] Vedant, and Allison, J. T., 2019, "Multifunctional Structures for Attitude Control," ASME Smart Materials, Adaptive Structures and Intelligent Systems, Louisville, KY, Sept. 9–11, p. V001T03A005. .
[21] Kalthof, R., 2014, "Multibody Dynamics Modeling of Flexible Aircraft Flight Dynamics.", Master thesis, TU Delft.
[22] Howell, L. L., Midha, A., and Norton, T., 1996, "Evaluation of Equivalent Spring Stiffness for Use in a Pseudo-Rigid-Body Model of Large-Deflection Compliant Mechanisms," ASME J. Mech. Des., **118**(1), pp. 126–131.
[23] Dado, M. H., 2001, "Variable Parametric Pseudo-Rigid-Body Model for Large-Deflection Beams With End Loads," Int. J. Non-Linear Mech., **36**(7), pp. 1123–1133.
[24] Lee, Y. H., Vedant, Ewoldt, R. H., and Allison, J. T., 2019, "Strain-Actuated Solar Arrays for Spacecraft Attitude Control Assisted by Viscoelastic Damping," Proceedings of the 13th World Congress of Structural and Multidisciplinary Optimization, Beijing, China, A230788.
[25] Wen, J. T., and Murphy, S., 1991, "Stability Analysis of Position and Force Control for Robot Arms," IEEE Trans. Automat. Control, **36**(3), pp. 365–371.
[26] Shamir, T., 1990, "The Singularities of Redundant Robot Arms," Int. J. Robot. Res., **9**(1), pp. 113–121.
[27] Vedant, PRBDM code repository. [Online]. https://github.com/VedantFNO/PRBDM_JMD.

[28] Smith, N. A., and Tromble, R. W., 2004, "Sampling Uniformly From the Unit Simplex," Johns Hopkins University, Technical Report No. 29.
[29] The MathWorks. Multistart algorithm. Accessed on June 10, 2019.
[30] Ugray, Z., Lasdon, L., Plummer, J., Glover, F., Kelly, J., and Martí, R., 2007, "Scatter Search and Local NLP Solvers: A Multistart Framework for Global Optimization," INFORMS J. Comput., **19**(3), pp. 328–340.
[31] Glover, F., 1998, "A Template for Scatter Search and Path Relinking," *Artificial Evolution*, H. J. Lutton, E. Ronald, E. Schoenauer, and M. S. Dominique, eds., Springer Berlin Heidelberg, pp. 1–51.
[32] The MathWorks. Paretosearch Algorithm. Accessed June 10, 2019.
[33] Fleischer, M., 2003, "The Measure of Pareto Optima Applications to Multi-Objective Metaheuristics," International Conference on Evolutionary Multi-Criterion Optimization, C. M. Fonseca, P. J. Fleming, E. T. Zitzler, and L. D. Kalyanmoy, eds., Springer, Berlin, Heidelberg, pp. 519–533.
[34] Custódio, A. L., Madeira, J. A., Vaz, A. I. F., and Vicente, L. N., 2011, "Direct Multisearch for Multiobjective Optimization," SIAM J. Optim., **21**(3), pp. 1109–1140.
[35] Plunkett, R., 1963, "Natural Frequencies of Uniform and Non-Uniform Rectangular Cantilever Plates," J. Mech. Eng. Sci., **5**(2), pp. 146–156.